Received: 11 May 2019 | Revised: 19 November 2019 | Accepted: 20 November 2019

DOI: 10.1002/mrm.28125

FULL PAPER

Magnetic Resonance in Medicine

Influence of contrast agent dispersion on bolus-based MRI myocardial perfusion measurements: A computational fluid dynamics study

Johannes Martens[1,2] | **Sabine Panzer**[1,2] | **Jeroen van den Wijngaard**[3,4] | **Maria Siebes**[3] | **Laura M. Schreiber**[1,2]

[1]Chair of Molecular and Cellular Imaging, Comprehensive Heart Failure Center, University Hospitals Würzburg, Germany

[2]Department of Cardiovascular Imaging, Comprehensive Heart Failure Center, University Hospitals Würzburg, Germany

[3]Department of Biomedical Engineering & Physics, Amsterdam University Medical Center, University of Amsterdam, Amsterdam Cardiovascular Sciences, Amsterdam, Netherlands

[4]Department of Clinical Chemistry and Hematology, Diakonessenhuis, Utrecht, Netherlands

Correspondence
Laura M. Schreiber, Comprehensive Heart Failure Center, University Hospitals Würzburg, Am Schwarzenberg 15, Haus A15, Würzburg 97080, Germany.
Email: schreiber_l@ukw.de

Funding information:
German Ministry of Education and Research; Grant/Award No. 01E1O1504

Purpose: Bolus-based dynamic contrast agent (CA) perfusion measurements of the heart are subject to systematic errors due to CA bolus dispersion in the coronary arteries. To better understand these effects on quantification of myocardial blood flow and myocardial perfusion reserve (MPR), an in-silico model of the coronary arteries down to the pre-arteriolar vessels has been developed.

Methods: In this work, a computational fluid dynamics analysis is performed to investigate these errors on the basis of realistic 3D models of the left and right porcine coronary artery trees, including vessels at the pre-arteriolar level. Using advanced boundary conditions, simulations of blood flow and CA transport are conducted at rest and under stress. These are evaluated with regard to dispersion (assessed by the width of CA concentration time curves and associated vascular transport functions) and errors of myocardial blood flow and myocardial perfusion reserve quantification.

Results: Contrast agent dispersion increases with traveled distance as well as vessel diameter, and decreases with higher flow velocities. Overall, the average myocardial blood flow errors are $-28\% \pm 16\%$ and $-8.5\% \pm 3.3\%$ at rest and stress, respectively, and the average myocardial perfusion reserve error is $26\% \pm 22\%$. The calculated values are different in the left and right coronary tree.

Conclusion: Contrast agent dispersion is dependent on a complex interplay of several different factors characterizing the cardiovascular bed, including vessel size and integrated vascular length. Quantification errors evoked by the observed CA dispersion show nonnegligible distortion in dynamic CA bolus-based perfusion measurements. We expect future improvements of quantitative perfusion measurements to make the systematic errors described here more apparent.

KEYWORDS

bolus-based perfusion measurement, computational fluid dynamics, magnetic resonance imaging, myocardial blood flow, myocardial perfusion reserve

1 | INTRODUCTION

Despite continuous improvement of prevention and therapy, cardiovascular diseases, and particularly coronary artery disease, represent the most frequent cause of death in industrial countries (about 17%).[1] Coronary artery disease is caused by arteriosclerosis of coronary arteries, a chronically progressing degeneration of vessel walls leading to vessel narrowing (stenosis) or occlusion, which can give rise to myocardial ischemia and infarction.[2]

Dynamic MRI before, during, and after the passage of a rapidly injected contrast agent (CA) bolus allows the assessment of pathologically induced changes in myocardial blood flow (MBF) or myocardial perfusion reserve (MPR) for clinical decision making,[3-6] whether induced by an epicardial stenosis or microcirculatory dysfunction.[7,8] Although most clinical perfusion MRI measurements are qualitative or semiquantitative (such as using the upslope technique), there is an increased interest in quantitative perfusion in terms of MBF in milliliters of blood per minute per gram of tissue or MPR. Tracer-kinetic models such as the Fermi-model[9] MMID4 (Multiple path, Multiple tracer, Indicator Dilution, 4 region model; National Simulation Resource, University of Washington, Seattle, Washington)[10,11] or Patlak plot analysis[12] allow the calculation of absolute MBF values. These techniques of tracer kinetic modeling are increasingly automated to improve their robustness and reproducibility.[13,14]

All bolus-based perfusion measurement techniques require exact knowledge of the temporal evolution of the CA bolus entering the voxel or region of interest (i.e., the arterial input function [AIF]). For technical reasons, the AIF cannot be quantified directly but is usually estimated in the left ventricle (LV).[15-17] Computational fluid dynamics (CFD) simulations—as they have been widely used for general interpretation of perfusion MRI data[18-21]—have shown that the CA bolus experiences dispersion during its passage through the epicardial vasculature toward the myocardial region of interest.[22-24] This widening is erroneously attributed to the microcirculation, and therefore leads to a systematic underestimation of the MBF and an overestimation of the MPR values. Interestingly, CFD simulations demonstrate that these effects occur even in nonstenotic (i.e., normal) vessels. Vascular stenosis introduces further complexity.[25]

These earlier studies suggest systematic MBF underestimation due to various influencing factors such as blood flow velocity, length, curvature, and branching of the analyzed vascular segment(s), as well as stenosis shape and degree. Furthermore, these studies indicate a decreasing influence of smaller vessels on dispersion, suggesting that the CA bolus dispersion effects do not occur in vessels beyond a certain limiting vessel generation.

In this work, for the first time an analysis of CA transport in the complete healthy porcine coronary vasculature, including both left and right coronary arteries down to the pre-arteriolar level, is performed. The use of high-resolution ex vivo 3D morphologic coronary tree geometries obtained from an imaging cryomicrotome[26] allows for the generation of a detailed in silico model of CA transport. Furthermore, to achieve realistic hemodynamic conditions, an advanced boundary condition (BC) is used, which includes coronary flow effects due to tissue pressure acting on the downstream microvasculature.[27]

The simulations are performed under physiological conditions of rest and stress. The calculated bolus dispersion and resulting systematic errors of MBF and MPR quantification from CA bolus-based MRI are analyzed with regard to vessel sizes and the distance to the vascular tree inlet.

2 | METHODS

2.1 | Segmentation of porcine coronary vasculature

The data source consists of a high-resolution imaging cryomicrotome data set of an ex vivo porcine heart (male domestic Yorkshire pig, ~30 kg).[26] In a procedure comparable to what is applied in Boutsianis et al,[28] the heart was arrested in diastole using the King's College London injection method; hence, the extracted 3D vascular models represent geometries where coronary flow is dominant. With the software package *SimVascular* (version 2, SimTK, simvascular.github.io[29]), 3D models of both the left coronary tree (LCT) and right coronary tree (RCT) starting at the left main and right coronary artery, respectively, are segmented from a high-resolution imaging cryomicrotome data set of an ex vivo porcine heart (male domestic Yorkshire pig, approximately 30 kg).[26] Vessel diameters down to 300 μm are included in this procedure (Supporting Information Video S1). Using the software packages *Meshmixer* (Autodesk, San Rafael, California) and *ICEM-CFD* (ANSYS, Canonsburg, Pennsylvania), the 3D geometries are carefully optimized and prepared for the simulations. This includes the creation of perpendicular outlet areas at the end of the segmented vessel

branches and naming of associated surface triangles (INLET, WALL, OUTLET1, …). Vessel bifurcations are smoothed using adequate coronary artery disease software, applying meticulous user intervention. Due to the high level of detail in the data sets, the total model creation and preparation takes several months to complete, although allowing analysis of much smaller vessels than in, for example, Boutsianis et al.[28]

2.2 | Volume discretization

The vascular geometries are discretized using the software package *cfMesh* (Creative Fields, London, United Kingdom), yielding mesh sizes of 13 830 835 (96% hexahedral type, duration mesh creation: 1.5 hours) on the LCT grid and 6 975 193 (95%, 20 minutes) on the RCT grid. The chosen resolution is based on the mesh convergence analyses in Refs[23,25,30,31].

2.3 | Computational fluid dynamics simulations

The CFD simulations are performed in a 2-step procedure with the open-source software package *OpenFOAM* version 2.3.0 (OpenCFD, ESI Group, Bracknell, United Kingdom) using the finite volume method. First, blood flow is calculated by solving the Navier-Stokes equation, as follows:

$$\rho\left(\frac{\partial \mathbf{u}}{\partial t}+\mathbf{u}\nabla\mathbf{u}\right)=\nabla p+\mu\Delta\mathbf{u}, \tag{1}$$

where ρ is the density, t is the time, $\mathbf{u}$ is the velocity, p is the fluid pressure, and μ is the fluid viscosity. Subsequently, the advection diffusion equation,

$$\frac{\partial c}{\partial t}=D\Delta c+\mathbf{u}\nabla c, \tag{2}$$

is solved to simulate CA transport based on the solution for $\mathbf{u}$ of Equation 1. Here, c denotes CA mass concentration in the fluid and D is its diffusion coefficient.

2.3.1 | Blood flow

Simulation of blood flow in the segmented 3D models requires a well-defined set of BCs. At the inlets, the volume flow curves from Figure 1A are applied. These are computed based on the electrical circuit analog of cardiac circulation (Figure 1B).[27] The obtained volume flow curves are in accordance with Refs[27,32,33] and include systolic retrograde coronary blood flow.[34]

In the circuit from Figure 1B, the pulsatile energy "stored" due to the microcirculatory compliance C during the time interval Δt is given by

$$p_C(t)=p_C(t-\Delta t)+\frac{1}{C}\int_{t-\Delta t}^{t}F\left(t'\right)dt' \tag{3}$$

$$\approx p_C(t-\Delta t)+\frac{\Delta t}{C}\cdot(F(t)-F(t-\Delta t)), \tag{4}$$

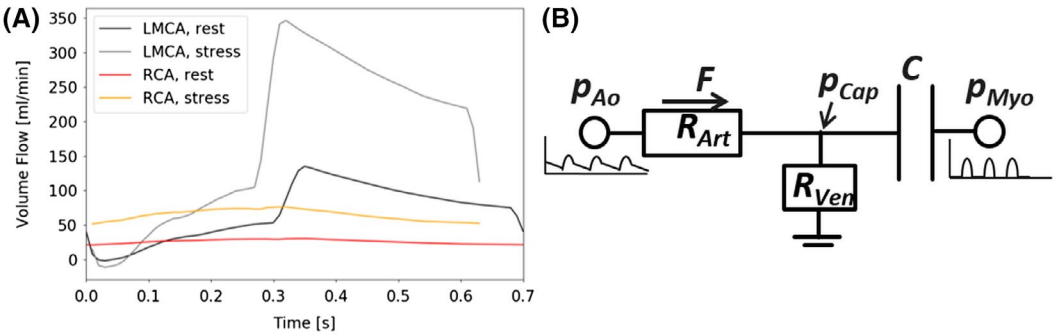

FIGURE 1 A, Volume flow curves assigned at the model inlets of the left main coronary artery (LMCA) and right coronary artery (RCA) for hemodynamic rest and stress states. The volume flow curves are computed using the analog model in (B). The curves used for the stress simulations are obtained by reducing the cardiac cycle duration by 10% and adapting the assigned resistance and compliance values. B, Electrical circuit analog of coronary blood circulation. The resistance R_{Art} and the capacitance C, corresponding to vascular flow resistance and vessel compliance within tissue, respectively, can be treated as assembeld in parallel (RC circuit), with applied voltages in terms of pressures p_{Ao} and p_{Myo}, representing the pressures in the aorta and the myocardium, respectively. The relation between the flow resistances in the arteries and veins, R_{Art}, R_{Ven}, and the compliance C of the myocardial vessels determine the blood flow F and the pressure at capillary level p_{Cap}. This model is used to generate the inflow curves shown in (A) as well as the capillary pressure curves that are used to calculate the outlet pressures at each time step of the computational fluid dynamics (CFD) simulations according to Equation 5. The approximation of the required parameters (R_{Art}, R_{Ven}, and C_{Myo}) and the outlet resistances is described in section 2.3.1

where $F(t)$, $F(t-\Delta t)$ denote flow through the vessel. Please note that vessel stiffness is only assumed for vessels larger than 300 μm, and not for the smaller vessels considered in these precalculations. Depending on the initial "charge" of the myocardial compliance, the system at some point reaches a stationary periodic state, which is computed iteratively. The initial aortic pressure curve is taken from Kamoi et al,[35] and the corresponding ventricular pressure curve is estimated within a physiologic range.[36] The duration of the cardiac cycle is scaled to 0.7 seconds, which yields a typical heart rate for pigs weighing 25-35 kg,[37] corresponding to the size of the animals from which the data set used here was extracted.[26]

The pressure p_{Cap} in Figure 1B represents the pressure in the middle of the capillaries. Thus, the resistances R_{Art} and R_{Ven} each comprise the capillary contributions. The shares of arterial (~0%), pre-/arteriolar (~60%), capillary (~25%), and venous vessels (~15%) are estimated according to their contributions to total flow resistance.[38,39] Depending on the 3D model's inlet radius, the total resistance is estimated according to Huo and Kassab.[40] Under physiological stress, the contributions of pre-arteriolar, capillary, and venous vessels to R_{Art} and R_{Ven} are adapted accordingly[39]: reductions by 86%, 0% and 98%, respectively.

Because no direct measurement of the parameter C within the surrounding tissue is possible, its value is adjusted in a sensitivity analysis to obtain physiologic volume flow curves. With the help of the open-source software package *QUCS* (*Quite Unified Circuit Simulator*),[41] the RC circuit from Figure 1B is established. The value of C is therefore adapted to yield realistic ratios of the mean right to left coronary flow (~1:4) and diastolic to systolic flow (~3:1).[36] These steps are performed before the CFD simulations.

The solutions for p_{Cap} are mapped onto the segmented 3D models to provide the CFD simulations with a well-defined set of BCs. The capillary pressure is scaled depending on the depth within the myocardium of the outlet under consideration.[42] For each model outlet, a downstream arterial resistance R_i is calculated according to the self-similarity of the coronary tree.[40,43-45]

Finally, for each time step t of the Navier-Stokes simulation, the pressure

$$p_i(t) = F_i(t) \cdot R_i + p_i^{Cap}(t) \quad (5)$$

is computed and assigned at outlet i, where F_i denotes outlet flow. This approach ensures that F_i adapt to the conditions within the 3D model. At the same time, the prevailing intramyocardial pressure and outlet hemodynamic resistances are taken into account. In comparison to previous works in which initially considerably simpler[22-24] and structured tree outlet BCs[25,30] were applied, this allows CFD simulations based on individual aortic pressure curves.

Subsequently, the solutions of the Navier-Stokes equations are stored for an entire cardiac cycle (~2 Mio files, 1-2 TB per case, a total of about 7-8 TB for 4 simulations: 2 models, 2 hemodynamic states). The following BCs are used to solve Equation 1. At the vessel walls, which are modeled to be stiff, a no-slip condition (velocity U = 0) is applied. Blood viscosity is modeled according to Ballyk's generalized power law,[46] and turbulences are incorporated using the dynamic Smagorinsky large-eddy simulation approach.[47] Blood is assumed to be incompressible with density $\rho = 1060$ kg/m^3. The results from the blood flow simulations and their physiological correctness have been assessed and discussed in Martens et al.[48] Serving as a means to subsequently perform CA transport simulations, these are not described in detail here.

2.3.2 | CA transport

In the second step of the simulations, the previously stored physical fields of the cardiac cycle are repeatedly read back to solve Equation 2 and compute the transport of a Gd-DOTA-chelate complex (diffusion coefficient D = 2.98E-10 m^{2}s^{-1}),[49] which is used commonly in quantitative myocardial perfusion MRI. This is performed for each hemodynamic state until a time of 50 seconds is reached (Figure 1), when it can be assumed that all CAs have left the system. Recirculation of blood and CA leaving the coronary 3D geometries is not modeled. We followed the general assumption that CA exchange between blood and extravascular space occurs predominantly in the capillaries with their thin endothelial layer[50] (i.e., not in the larger vessels considered in our CFD simulations, which have thicker vessel walls).

Contrast agent inflow at both inlets is modeled by a γ-variate function $C_{CA}(t) = a\left(t - t_0\right)^b e^{-c(t-t_0)}$, (a = 1.013E-4; b = 2.142; c = 0.454 s^{-1}), a stochastic representation of a realistic concentration time curve in the LV.[51]

2.4 | Computational facilities

All simulations are performed on the High Performance Computing cluster *CoolMUC-2* at the Leibniz Supercomputing Center (LRZ) (Munich, Germany). The computations on the LCT and the RCT model are performed in parallel on 140 and 56 cores, respectively. The required computation times are about 2 days on both models for each hemodynamic state (total of 8 days).

2.5 | Analysis of CA transport

Contrast agent dispersion is investigated as a function of vessel diameter and integrated distance in the 3D vascular tree

geometries. For this purpose, CA concentration time curves at several points along the large epicardial arteries and at all outlets are analyzed.

According to Calamante et al,[52] dispersed AIF_{disp} are related to the AIF_{LV} using the following mathematical convolution:

$$AIF_{disp}\left(t-t_0\right)=AIF_{LV}\left(t\right)\otimes VTF\left(t-t_0\right), \quad (6)$$

where the vascular transport function (VTF) comprises dispersion effects. The parameter t_0 is the start time of CA inflow at the inlet.

By use of zeroth, first, and second momentum of $AIF_{disp,LV}$, the VTF's SD and mean vascular transit time (MVTT) can be calculated without deconvolution of Equation 6 as follows[23,52]:

$$MVTT\equiv\frac{VTF^{(1)}}{VTF^{(0)}}=\frac{\int t\cdot VTF\left(t\right)dt}{\int VTF\left(t\right)dt}=\frac{AIF_{disp}^{(1)}}{AIF_{disp}^{(0)}}-\frac{AIF_{LV}^{(1)}}{AIF_{LV}^{(0)}}, \quad (7)$$

$$SD_{VTF}\equiv\sqrt{\frac{\int\left(t-MVTT\right)^2\cdot VTF\left(t\right)dt}{\int VTF\left(t\right)dt}} \quad (8)$$

$$=\sqrt{\frac{AIF_{disp}^{(2)}}{AIF_{disp}^{(0)}}-\frac{AIF_{LV}^{(2)}}{AIF_{LV}^{(0)}}+\left(\frac{AIF_{LV}^{(1)}}{AIF_{LV}^{(0)}}\right)^2-\left(\frac{AIF_{disp}^{(1)}}{AIF_{disp}^{(0)}}\right)^2} \quad (9)$$

The integral momenta $f^{(i)}$ are approximated by Riemann sums over all N time steps t_k with intervals Δt, $f^{(i)}=\sum_k^N\left(t_k\right)^i f\left(t_k\right)\Delta t$. In addition, the SDs of the AIF_{disp} are used for the analysis:

$$SD_{AIF}\equiv\sqrt{\frac{\int\left(t-\overline{T}\right)^2\cdot AIF\left(t\right)dt}{\int AIF\left(t\right)dt}} \quad (10)$$

with mean arrival time $\overline{T}$. By definition, $\overline{T}$ is shifted from MVTT by $AIF_{LV}^{(1)}/AIF_{LV}^{(0)}$.

As defined in Refs [11] and [53], the relative dispersion (RD) is given as

$$RD_{VTF,AIF}=\frac{\sigma}{\bar{t}}, \quad (11)$$

where $\bar{t}=MVTT,\overline{T}$ and $\sigma=SD_{VTF},SD_{AIF}$, respectively. For volume flow F through a vascular volume V, the central volume theorem is used[53,54]:

$$\sigma\propto\bar{t}=V/F, \quad (12)$$

which can be set up making RD a dimensionless constant characterizing a particular vascular bed. Even though the results from Martens et al[31] shed doubt on the question of whether vascular systems as they are considered here fulfill the requirements for indicator dilution theory (e.g., linear system, well-mixed compartment[54]), in this work, $RD_{VTF,AIF}$ is used nonetheless for parametrization of observed dispersion.

2.6 | Estimation of quantification errors

By using the tissue perfusion model MMID4, the CA concentration time curves are used to compute the ΔMBF values. The workflow depicted in Figure 2 is used to make an approximation based on the AIF_{disp}. Thus, comparison of MBF_{Fit} and the assumed generic value MBF_{Gen} allows analysis of MBF quantification errors as follows:

$$\Delta\mathrm{MBF}=\frac{\mathrm{MBF}_{Fit}-\mathrm{MBF}_{\mathrm{Gen}}}{\mathrm{MBF}_{\mathrm{Gen}}}. \quad (13)$$

The parameters to generate tissue concentration time curves $Conc_{Myo}$ from Figure 2 with MMID4 can be set within the software *JSim*[55] and are chosen as in a number of other studies.[6,9,10,22-25,30,56] At rest, an MBF of 1 mL/min/g is assumed. At stress, MBF is assumed to increase to 2.7 and 2.3 mL/min/g in the LV and RV, respectively. This

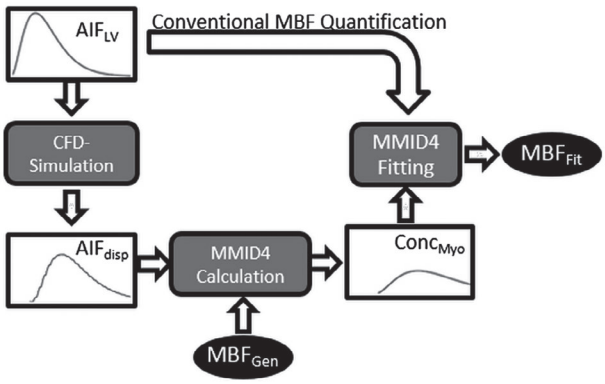

FIGURE 2 Workflow to estimate change in myocardial blood flow (ΔMBF). Arterial input function (AIF) from the left ventricle (AIF_{LV}) is used as the input boundary condition (BC) in the CFD simulations and delivers the dispersed (real) AIF_{disp} in the providing vessel. Combined with a generic MBF_{Gen} and MMID4, this yields a myocardial tissue concentration curve $Conc_{Myo}$, which is subsequently used as a synthetic myocardial MRI perfusion measurement, and which allows for the calculation of MBF_{Fit} using AIF_{LV} and making use of the MMID4 (Multiple path, Multiple tracer, Indicator Dilution, 4 region model) like in a quantitative perfusion MRI study. Comparison of MBF_{Fit} and MBF_{Gen} is then used to estimate the systematic error ΔMBF

corresponds to the overall increase of the volume blood-flow curves from Figure 1A (i.e., a homogeneous MPR = MBF_{stress}/MBF_{rest} = 2.7 [2.3] in the LV [RV], respectively, is presumed).

The subsequent MBF calculation is performed with the fitting algorithm SENSOP[57] within JSim, a modification of the well-known Levenberg-Marquardt algorithm.[58] Fitting with MMID4 is performed with 4 free parameters[6,10,59,60]: plasma flow F_P (MBF) 0-7 mL/g/min, permeability surface area product v_{PSg} 0.25-8 mL/min/g, plasma volume V_p 0.05-0.09 mL/g, and the bolus delay −1 to 3 seconds. All other parameters are kept constant.

After calculation of $\Delta MBF_{Rest,Stress}$, ΔMPR is calculated as

$$\Delta MPR = \frac{MPR_{Fit} - MPR_{Gen}}{MPR_{Gen}}, \quad (14)$$

where $MPR_{Fit} = MBF_{Fit,Stress}/MBF_{Fit,Rest}$ and MPR_{Gen} = 2.7 and 2.3 for LV and RV, respectively. Errors of ΔMBF and ΔMPR are calculated by Gaussian uncertainty propagation of the standard errors from the MMID4 fitting.

3 | RESULTS

3.1 | Quantification of CA dispersion

Figure 3C-H shows the evolution of MVTT, SD_{AIF}, and SD_{VTF} (Equations 4-6) at rest along various vessel segments. The MVTT increases monotonically in all branches of both trees. Results in several vessels show elevated MVTT values in distal parts when compared with the other branches (LCT: diag2, diag3, terminal left anterior descending [LAD] branches; RCT: 1, 4, 7). Similarly, branches with more pronounced MVTT increase also show higher increase of SD_{VTF} and SD_{AIF} at the same locations.

Nonetheless, $SD_{VTF,AIF}$ shows a qualitatively different behavior than MVTT, as this parameter even decreases in some branches. For example, diag2 and diag4 show distinct SD_{VTF} reductions downstream of approximately 35 mm and 50 mm, respectively. These positions coincide with the first cross section after the bifurcation of the 2 branches from the LAD (indicated in black in Figure 2A). Further downstream, SD_{VTF} increases again. The behavior in the proximal LAD at these positions is opposed to this and shows stronger increase in SD_{VTF} right after the bifurcation. This is particularly apparent in the LAD downstream of the bifurcation of diag4.

Table 1 lists the maximum and average MVTT and $SD_{VTF,AIF}$ values (arithmetic mean, SD). Dispersion in the RCT is enhanced compared with the LCT. This is due to the fact that, in general, larger volume flows (Figure 1A) in the LCT result in markedly higher flow velocities than in the RCT. Higher flow velocities have similar effects as an increased diffusion coefficient, causing reduced dispersion.[23,24]

3.2 | Contrast agent transport mechanisms

Figure 4 shows different phases of the CA passage through the coronary trees. For better visualization, a temporally shortened bolus (factor 100) is used here. In the LCT, CA passes large parts of the left circumflex artery tree before it reaches distal segments in the LAD tree. In the RCT, transport is considerably slower (Supporting Information Videos S2 and S3). After a short time, maximum concentrations in the LCT are well below those observed in the RCT (Figure 4, time step 1.85 seconds). The bolus front is spatially more spread in the LCT than the RCT. This may also be a result of the higher simulated flow velocities in the LCT, causing increased longitudinal diffusion-like effects.[61]

Figure 5A illustrates CA transport at the bifurcations to diag3 and diag4 from the proximal LAD. The CA moves faster to diag4 than to diag3. This behavior is also reflected in the decreased MVTT and $SD_{VTF,AIF}$ in diag4, compared with diag3 (Figure 3C,E,G). Dispersion along the proximal LAD, the most unidirectional vessel, is also moderately increased, comparable to diag3 (Supporting Information Video S4). Figure 5B shows the velocity streamlines in the bifurcation. Highest flow velocities are obtained in diag4, where the MVTT and $SD_{VTF,AIF}$ increase is smaller. Furthermore, streamlines feeding into this branch originate from central luminal LAD segments, whereas diag3 is only fed from streamlines near the LAD vessel wall, where flow velocities are lower than at the vessel center.

The results depicted in Figures 3-5 reflect the influencing factors on CA dispersion. Similar observations were made previously in synthetic or less detailed studies.[31] Due to the inhomogeneous CA distribution across the vessel lumen, CA transport at bifurcations is strongly influenced by the branching angle and by the orientation of the daughter vessels with respect to the curvature of the upstream vessel (Figure 4). For example vessels diag4 and branch 2 have "opportunist" positions where CA transport takes place faster than in neighboring vessels. Furthermore, flow velocities in the neighboring branches are also smaller than in diag4 and branch 2, which, according to earlier studies in simple test geometries,[24] results in more pronounced bolus dispersion.

3.3 | Relative dispersion analysis

The results depicted in Figure 6 show different dependencies of $RD_{VTF,AIF}$ on vessel diameter and distance traveled in the coronaries. Qualitatively, as expected, the parameters increase with increasing diameter. The behavior does not differ

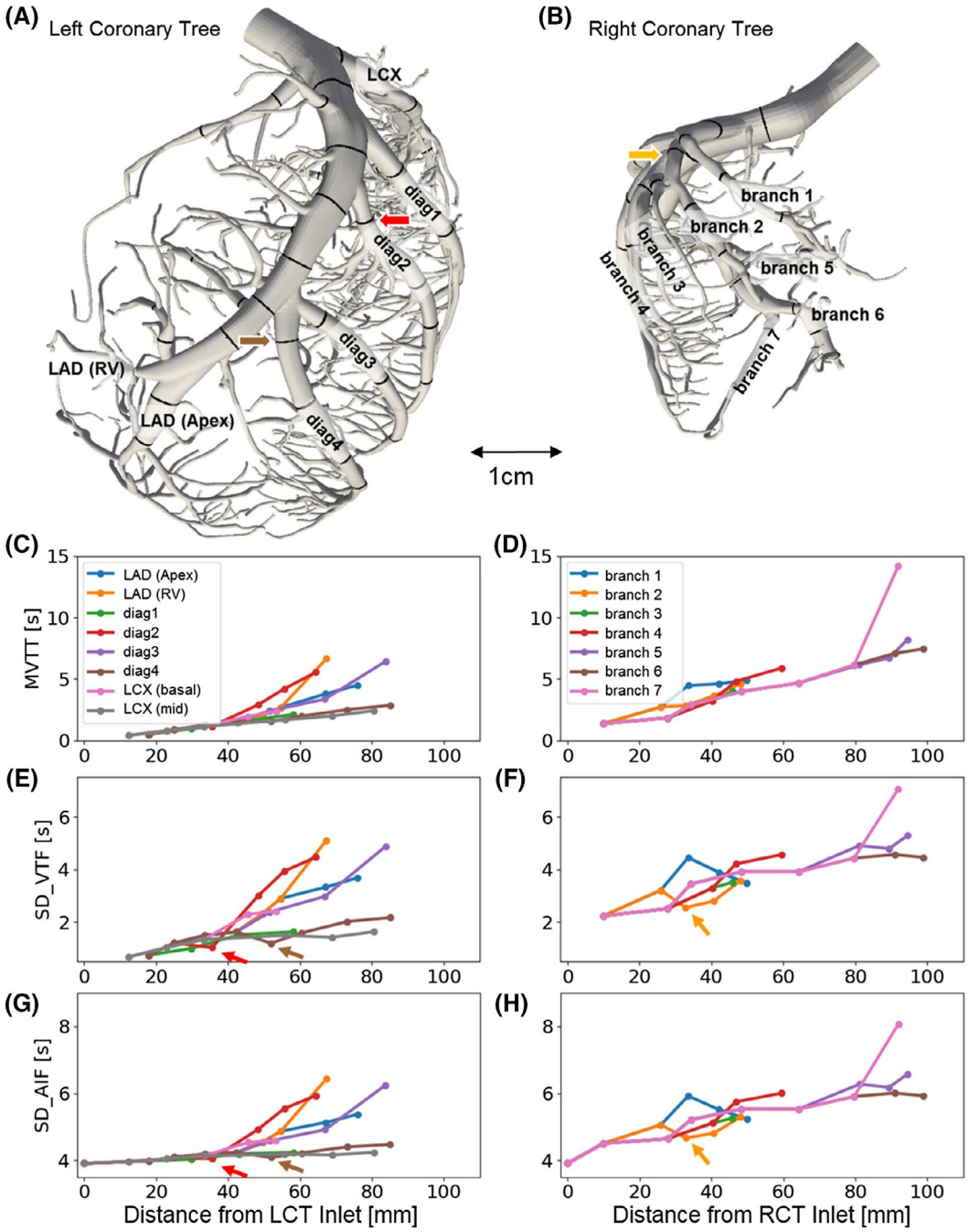

FIGURE 3 Evolution of MVTT, SD of the vascular transport function (SD_{VTF}), and SD_{AIF} along single branches of the 3D models. The data points represent the values obtained from Equations 4-6 at the cross sections marked (A) and (B). In both coronary trees, MVTT increases monotonously. C-H, Behind bifurcations, at the positions marked by the red, brown and orange arrows (E-H), the SD_{VTF} and SD_{AIF} show distinctively reduced values when compared with the other vessels forming the bifurcation. Abbreviations: diag, diagonal branch; LCT, left coronary tree; LCX, left circumflex artery; RCT, right coronary tree; RV, right ventricle

strongly between rest and stress states; however, the slopes of the linear relationships do vary (Figure 7).

From a mathematical point of view, the general behavior of the scatter plots in Figure 6 can be analyzed using the definition of $RD_{VTF,AIF}$ (Equation 11). With increasing distance from the inlet, MVTT and $\overline{T}$ increase monotonically (Figure 3C,D). Figure 6 suggests that the associated $SD_{VTF,AIF}$ values do not increase at the same rate. Consequently, $RD_{VTF,AIF}$ gets smaller with integrated distance. Because larger vessel diameters will naturally be found more proximally, both MVTT and $\overline{T}$ are generally smaller there, resulting in larger $RD_{VTF,AIF}$ at smaller distances and, accordingly, larger diameters. Similarly, under hyperemic conditions, higher flow velocities result in reduced MVTT and $\overline{T}$, hence overall increasing RD (Figure 7C).

TABLE 1 Average and maximum values of MVTT, SD_{VTF}, and SD_{AIF} in the 3 coronary trees

Artery	MVTT (seconds)	SD_{VTF} (seconds)	SD_{AIF} (seconds)
A, Arithmetic mean values and SDs			
LCT	2.5 ± 1.6	2.3 ± 1.2	4.6 ± 0.7
LCX tree	1.4 ± 0.7	1.3 ± 0.3	4.1 ± 0.1
LAD tree	2.8 ± 1.7	2.4 ± 1.3	4.7 ± 0.7
RCT	4.9 ± 3.3	3.7 ± 1.1	5.5 ± 0.8
B, Maximum values			
LCT	6.6	5.1	6.4
RCT	14	7.1	8.1

Note: In the LCT, the maximum value is obtained in the most distal LAD branch leading to the right ventricle, and in the RCT, the maximum value is obtained in branch 6.

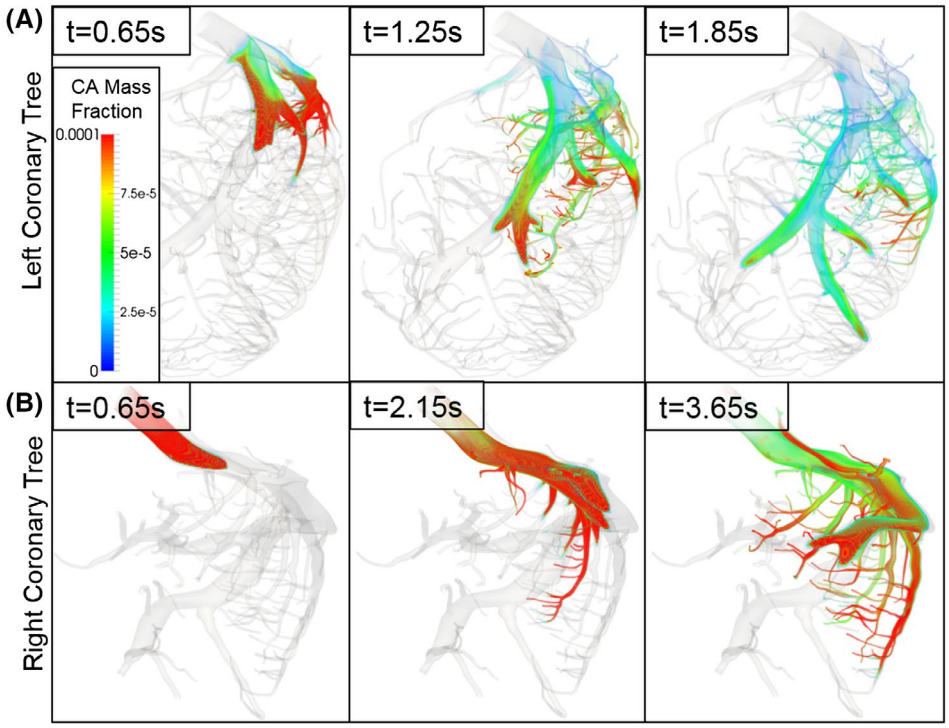

FIGURE 4 Contrast agent (CA) transport in LCT and RCT (*c* denotes the CA mass fraction, and the scale on the left applies for all screenshots). Top: Transport through the LCT (anterior view [Figure 3]). The CA reaches the distal parts of the left anterior descending (LAD) only after it has already passed large parts of the LCX (top right and in the background). Furthermore, it becomes obvious how CA distributes inhomogeneously into the different branches of the LAD (particularly diag3 and diag4 from Figure 3 in the middle of the screenshots [Figure 5]). Bottom: Transport through the RCA (inferior view [Figure 3]). Due to the lower blood flow velocities in the RCA, CA transport takes place over a longer time period than in the LCT, as seen by the comparison of the visualized time steps

The overall mean value (all vessels, rest and stress) of $RD_{VTF} = 0.57 \pm 0.25$ is in agreement with available literature values of the cardiovascular bed, which shows great variability (e.g., values of 0.38 ± 0.05[53] and 0.70 ± 0.07[62] have been found).

We can infer from Figure 6 that more pronounced bolus dispersion occurs in large vessels than in small vessels. The decrease of $RD_{VTF,AIF}$ with increasing vessel diameter implies that $SD_{VTF,AIF}$ is not proportional to MVTT ($\overline{T}$, respectively) for varying vessel diameters. With increased distance, vessel diameters become smaller, resulting in monotonically increasing MVTT (Figure 3A,B) and $\overline{T}$. However, due to the complexity of CA transport within the geometry (Figures 4 and 5, Supporting Information Videos S2-S4), $SD_{VTF,AIF}$ underlie strong heterogeneous influences along the vessel paths (Figure 3E,F), causing less pronounced increases of $SD_{VTF,AIF}$. As shown in Figures 4 and 5, reduced dispersion in smaller vessels is by no means exclusively due to reduced vessel sizes. On the contrary, these findings confirm the observations of an earlier pilot study[31] that bolus dispersion is strongly heterogeneous and depends on several different factors such as vessel bifurcations, branching angles, and

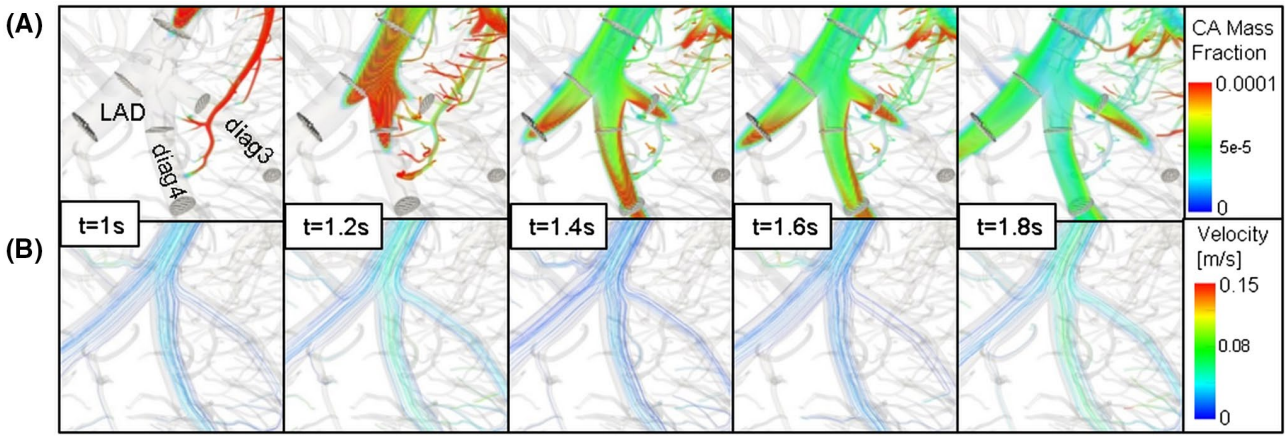

FIGURE 5 Anterior view of CA transport and velocity streamlines at the bifurcations into diag3 and diag4 from the LAD. Top: The CA first enters the diag4, which bifurcates at a more beneficial angle from the LAD than the diag3 with a steeper branching angle. Moreover, because of the upstream curvature of the large LAD, CA accumulates at the side where the ostium of the diagonal vessels 3 and 4 are located. The gray ovals in the path of the vessels represent the relevant cross sections from Figure 3A, at which MVTT and SDs are calculated (Figure 3). Ripples in the CA flow (e.g., at t = 1.2 seconds) are artifacts from the underlying computational grid. Bottom: The seed of the displayed streamlines is a sphere at the center of the LAD at the upper end of the depicted model section. Velocity streamlines show how different intraluminal segments "feed" into the branching vessels. Highest flow velocities are reached in diag4, where in the 3 depicted branches, the bolus dispersion is lowest

intraluminal CA concentration inhomogeneities due to shape variations of vessels in coronary trees.

3.4 | Magnetic resonance imaging quantification of ΔMBF and ΔMPR

Overall, $\Delta MBF_{Rest,Stress}$ values vary widely across the analyzed geometries (Table 2), with ΔMBF_{Stress} values being substantially smaller than ΔMBF_{Rest} values. Because the variation of ΔMBF_{Stress} is smaller than that of ΔMBF_{Rest}, the resulting ΔMPR is also subject to great variability. Considering the 3 large coronary territories, errors are largest in the RCT where the smallest flow velocities occur, and smallest in the left circumflex artery, which is traversed fastest by the CA.

To analyze the quantification errors regarding the traveled distance, the maximum distance range is subdivided into 6 segments of approximately 2 cm length each (Figure 8). A clear trend toward larger ΔMBF with increasing distances is obvious. As a consequence of the decreasing relationship between RD_{AIF} and integrated distance (Figure 6D), one would expect asymptotic behavior of $\Delta MBF_{Rest,Stress}$. This behavior can be observed in Figure 8 if the last 2 distance segments of the coronary trees are considered for the resting state simulations (segments 6-8 and 8-10 for the left circumflex artery, and 8-10 and 10-12 for the remaining trees). Weaker additional MBF underestimation is obtained between these 2 segments. However, looking at the results for the stress simulations, the relative increase between the last 2 distance segments is comparably higher. This results in what can be interpreted as a starting asymptotic behavior of ΔMPR toward larger traveled distances, in accordance with Sommer et al.[30] Comparing the behavior of the rest and hyperemic perfusion quantification errors with the results obtained for RD_{AIF} from Figure 6F,H, this is expected. The flatter slope of RD_{AIF} at stress with respect to the integrated distance indicates that under stress the relative contribution of distal vessels to CA dispersion is increased in comparison to the rest condition.

4 | DISCUSSION

We present results underlining our hypothesis that MBF quantification by dynamic bolus-based MRI measurements is subject to nonnegligible systematic errors. The estimation of perfusion quantification errors shows a clear tendency to increasing errors with longer traveled distance. Due to the reduced additional dispersion in smaller vessels under stress conditions in comparison to resting state, MPR quantification errors appear to be less pronounced at more distal positions. Averaged over all outlets and cross sections, MBF underestimation by $\Delta MBF_{Rest} = -28\% \pm 16\%$ and $\Delta MBF_{Stress} = -8.5\% \pm 3.3\%$) is obtained. Accordingly, an average MPR overestimation $\Delta MPR = 26\% \pm 22\%$ is observed.

Two factors are identified as major determinants for prediction of CA bolus dispersion and subsequent estimation of perfusion quantification errors:

- The distance traveled by the CA bolus; and
- The general magnitude of flow velocities in the considered vascular tree (Figures 4, 5, and 8).

However, as CA dispersion is strongly influenced by several factors (e.g., presence of vessel bifurcations, branching angles, intraluminal CA concentration inhomogeneities), an

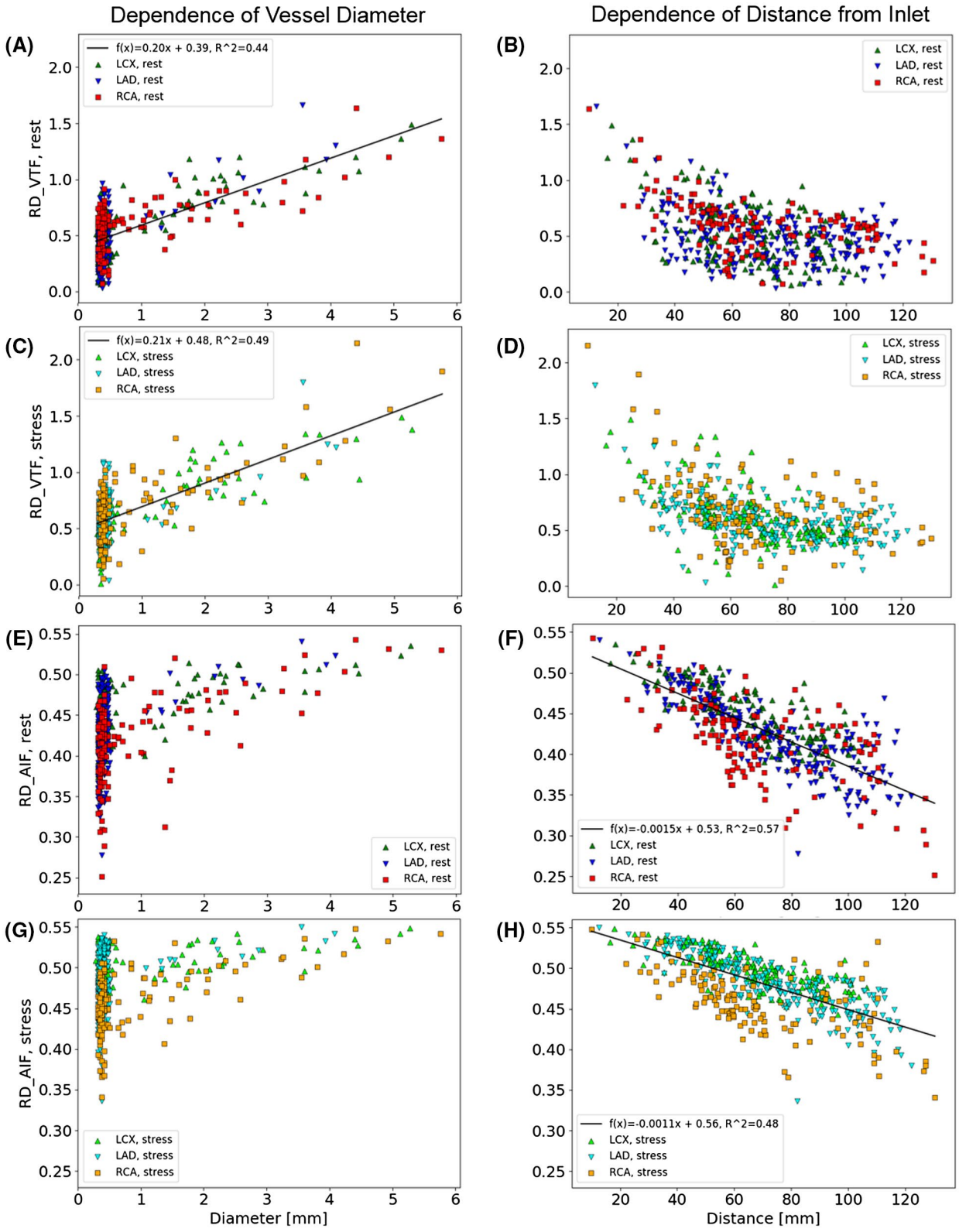

FIGURE 6 Dependence of relative dispersion (RD_{VTF} and RD_{AIF}) on vessel diameter and integrated distance at rest and under stress. A-D, The RD_{VTF} shows linearly increasing behavior in dependence of the vessel diameter for both hemodynamic states. Asymptotically decreasing behavior is obtained for RD_{VTF} dependence on the traveled distance. Under stress, the obtained RD_{VTF} appears to be generally higher. E-H, The RD_{AIF} spans a large range at smaller diameters (approximately 0.25-0.50 at rest and 0.35-0.55 under stress) and asymptotically increases for larger vessels. A linear decrease of RD_{AIF} with the integrated distance is observed, with a steeper slope at rest than under stress. Results from linear fitting within each coronary tree are shown in Figure 7

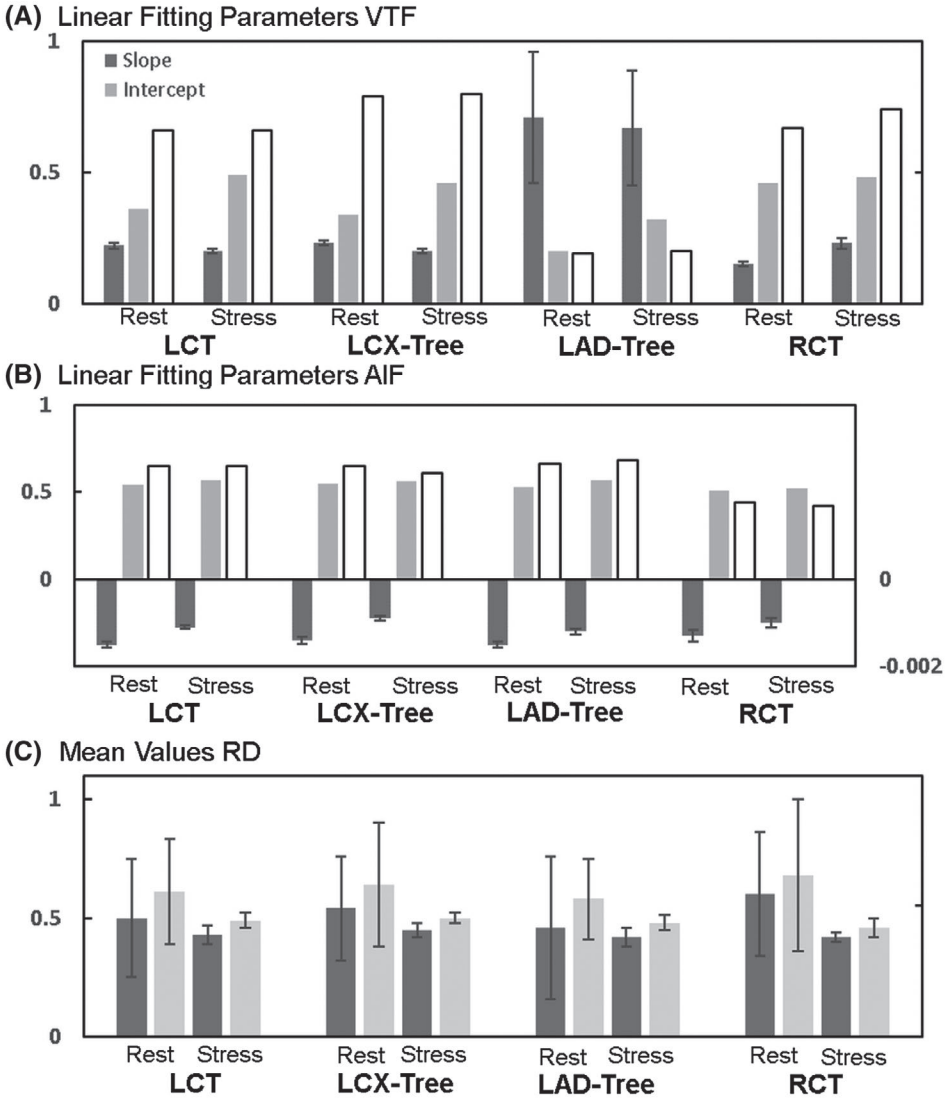

FIGURE 7 Linear regression parameters and mean RD in the coronary trees. A, Parameters for linear fitting of RD_{VTF} against the vessel diameter. B, Parameters for linear fitting of RD_{AIF} against the integrated distance. C, Obtained mean values of RD_{VTF} and RD_{AIF} over all cross sections and model outlets within each coronary tree. In (A)-(C), the error bars represent the standard error of the fitted slope and the SD, respectively

TABLE 2 Obtained ΔMBF_{Rest}, ΔMBF_{Stress}, and ΔMPR averaged over all vessels and within the large coronary arteries

Artery	ΔMBF_{Rest}	(%)	ΔMBF_{Stress}	(%)	ΔMPR	(%)
All	−28 ± 16	(−0.7)	−11 ± 12	(−2.0)	26 ± 22	(1.6)
LCT	−22 ± 14	(−1.1)	−7.5 ± 7.6	(−2.4)	24 ± 20	(1.9)
LCX tree	−17 ± 8	(−0.3)	−4.7 ± 3.5	(−1.5)	16 ± 8.8	(0.8)
LAD tree	−27 ± 16	(−0.8)	−9.3 ± 8.8	(−2.0)	29 ± 24	(1.4)
RCT	−41 ± 14	(−0.2)	−23 ± 14	(−1.1)	34 ± 22	(1.0)

Note: Errors are arithmetic SDs. The values in brackets represent the skewness (third momentum) of the distributions (unitless quantity).

error correction scheme based on these indicators would still be subject to large uncertainties. Nonetheless, considering that quantitative MRI perfusion measurements of this type are integrated more frequently in clinical diagnostics in the future, these quantities should be central to such a framework.

Our findings are in accordance with earlier results in simpler geometries,[23,24] where higher flow velocities were found to have similar effects on CA dispersion as an increased diffusion coefficient (i.e., resulting in reduced bolus dispersion). Moreover, transport phenomena as they were already

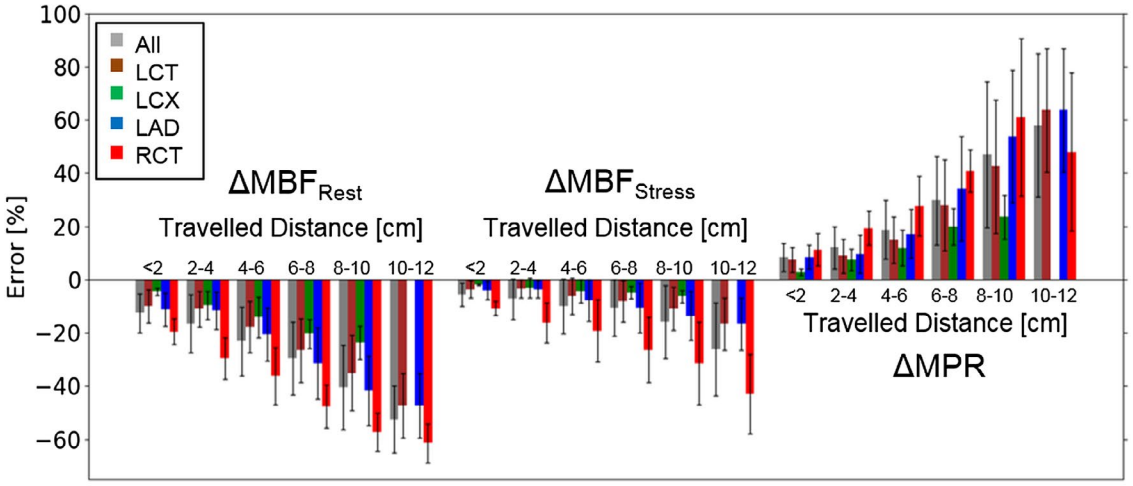

FIGURE 8 Increasing mean ΔMBF and change in myocardial perfusion reserve (ΔMPR) at different distances from the model inlet. In the last distance segment, there is no value for LCX

observed in Martens et al[31] are also found in these highly detailed coronary trees, underlining the complexity of CA dispersion in coronary arteries. Our observation that $RD_{VTF,AIF}$ depends strongly on vessel diameter, and integrated distance corroborates the hypothesis from previous analyses,[25,30] which proposed a reduced influence of ever smaller vessels on CA bolus broadening. In other words, transport processes in the large arteries have the dominant effect on CA dispersion.

Our initial assumption of the existence of a limiting vessel generation beyond which no more dispersion would occur, appears unrealistic considering the results described here. To clarify this further, validation on even more detailed cardiovascular geometries will be required. At present, we assume that the contribution of smaller vessels to overall bolus dispersion approaches zero asymptotically. In agreement with the previously performed CFD studies,[23,30] the reduced MBF underestimation at stress results in MPR overestimation. This is in contrast to an initially performed mathematical analysis of CA dispersion,[60] where the assumption was made that AIF dispersion from the LV to the tissue can be modeled by a mathematical convolution of the AIF_{LV} with a VTF. Because no prior knowledge existed, an exponential VTF was assumed in that study to yield a general insight regarding the influence of bolus dispersion on myocardial perfusion estimates, demonstrating the basic observation that AIF bolus dispersion results in systematic errors of MBF values. The substantial differences between the findings may be due to the fundamentally different approaches.

The present analysis does not allow for direct verification of the simulation results with parallel MRI measurements; however, an indirect validation is possible. Comparison of the estimated MBF errors with experimental data obtained in animals by the microspheres method[63] or clinical data from PET and CT myocardial perfusion measurements in humans[64] permits general assessment of the simulation results. Particularly, the microsphere method is considered the experimental gold standard for the measurement of the spatial distribution of MBF. Moreover, the microsphere technique does not depend on the acquisition of dynamic data; therefore, dispersion-related quantification errors are less likely, despite potential minor issues at moderate to small spatial scales.[65]

In fact, several MRI studies reported an underestimation of MBF.[3,66-73] In those studies, the MBF values were analyzed with regard to issues of quantification algorithms,[69] applied MRI signal intensity corrections,[70] interstudy repeatability,[71] or motion correction.[72] For hyperemia, MBF underestimation was more pronounced in comparison to microsphere perfusion measurements[70,73]; however, it is well-known that the microsphere technique somewhat overestimates MBF in regions of high flow, and underestimates MBF in regions of low flow.[74] In general, the observation in those studies that quantitative perfusion MRI somewhat underestimates MBF compared to the microsphere technique agrees well with our simulation results. Nonetheless, the data vary considerably among studies using the microsphere technique. It is generally accepted that endocardial, midmyocardial, epicardial, as well as overall averaged absolute perfusion values by MRI and microspheres demonstrate good agreement[3,66,69,70,73] if statistical errors are taken into account.

We expect, however, that with further improvements of quantitative perfusion measurements, the systematic errors described here will become more apparent in the data, especially if spatial resolution and noise reduction are improved. This would allow a more profound investigation of transmural MBF differences.[75,76] It is well-known from the seminal papers of Bassingthwaighte[63,74,77] that the MBF distribution is highly inhomogeneous and obeys fractal relationships.

Because imaging measurements and pixel-by-pixel analysis usually introduce relatively high pixel noise, most PET, CT, and MRI studies average the analysis according to segments.[78-81] At this stage, it is unclear how much noise is introduced by imaging processes. Moreover, model fitting or deconvolution to noisy signal time curves may also introduce noise. It is yet unknown how much of the observed variation on a pixel-by-pixel level is physiologic in terms of MBF heterogeneity, and how much is related to the measurement and analysis process. It will be the aim of future studies to address these questions. This would allow us to clarify the reasons for MBF underestimation in MRI perfusion measurements in comparison to microsphere measurements. In other words, light can be shed on the question of whether the observed differences between the measurement techniques are due to the overestimation of MBF by the microsphere method, or due to CA bolus dispersion effects analyzed in this work—or possibly a combination of both.

Although perfusion measurements using PET also rely on dynamic imaging of tracer uptake in the tissue and supposedly are also subject to systematic errors similar to those observed here, they are considered the *clinical* gold standard. The comparison of our results with existing PET data is also not straightforward. In Miller,[17] several MRI quantification algorithms are compared and, in general, at higher MBF values, MRI underestimates MBF in comparison to PET. Overall, in Refs [17] and [82], a general MBF underestimation by MRI was observed. On the other hand, Fritz-Hansen et al[83] found MBF underestimation by MRI under stress in comparison to PET quantification, and good agreement for resting conditions.

Even though in several of these studies the obtained MBF values are calculated on a regional[69,71-73,75] or pixel-by-pixel basis,[3] an association of the quantified tissue voxel or segment with a specific coronary flow territory is not performed. Hence, an assessment of quantified MBF values in relation to the distance traveled by CA between the locations of AIF and perfusion quantification is difficult. As such, varying MBF values at the pixel level—as they are also observed in the healthy vasculature[3]—could possibly be ascribed to heterogeneous CA transport processes and subsequent systematic MBF quantification errors, as described in this work. To investigate this hypothesis in more detail, future studies are required to directly validate the CFD simulations. This could be achieved by parallel MBF quantification by MRI and microspheres in combination with the acquisition of morphological information of coronary vasculature and precise monitoring of hemodynamic and physiological conditions during the measurements.

Regarding the comparability of the porcine data set used here with the human cardiac vasculature, it should be pointed out that the pig's heart-to-body weight ratio is similar to that of an adult human,[37] and that the pig's heart shape is comparable to that of humans. It is therefore conceivable that effects described here will occur in humans as well, possibly to a different degree. The complexity of the observed processes suggests that interindividual differences are likely. Depending on the exact individual morphology, strongly heterogeneous CA bolus dispersion and subsequent MBF underestimation is therefore expected. This heterogeneous behavior is also reflected in the varying findings from the comparison studies discussed previously.

A simplifying assumption made in our study is that of stiff vessel walls in the blood flow simulations. The coronary vasculature is subject to strong deformations, in both the vessels' lumina and positions. The electrical analog of coronary circulation allows us to incorporate some of these effects in the outlet BCs. Although several authors found only a small influence of vessel motion and wall elasticity on blood flow modeling,[84-86] the extent of their impact on CA and particle transport requires additional analysis.[87] This could be done by integrating fluid–structure interaction methodology in the simulations, although at the cost of considerably increased computational demands. In CFD simulations, re-entering of blood at the inlet or CA leaving the geometries at the outlets (i.e., effects of second pass of CA) are generally ignored. The assumption that all CA has left the system at 50 seconds is applicable here, as no exchange between extravascular interstitial space and the blood stream is included. This is considered in the subsequent calculation of ΔMBF with MMID4. Using fluid–structure interaction, this could be integrated in future analyses as well, which would further increase computational demands.

In addition to these limitations, the following should be noted. A γ-variate shape of the AIF at the model inlets is assumed in our simulation, neglecting potential bolus dispersion between the LV and the coronaries' orifices in the aorta. It is unclear to what extent this additional effect may modify bolus dispersion. We hypothesize that the additional bolus dispersion may be small, s the CA is well-mixed with the blood. Modeling of tracer transport above the aortic valve was beyond the scope of our study and may be investigated in the future. Moreover, with this approach, a homogeneous CA distribution is applied across the whole inlet lumen. Consequently, effects of heterogeneous CA distribution across the aortic lumen on CA inflow at the inlets of the LCT and RCT models are not considered. The simulations could be extended by integrating an aorta segment. However, it should be kept in mind that such an extension would come along with further difficulties in computational modeling due to an even larger span of vessel generations covered in the models.

Overall, our findings hold important implications for all bolus-based methods of perfusion quantification (e.g., MRI, PET, CT) as well as general particle or mass transport in the blood stream (e.g., drugs, medication). The extent of the influence of CA dispersion on quantified absolute MBF values may vary considerably among the different methods and could even hold positive effects on limitations of particular

methods. For example, distortions of the myocardial tissue response function due to the subvoxel intravascular fraction of fully saturation-recovered blood signal may be of reduced significance due to the dispersion effects discussed here. Nonetheless, because the total MRI signal variation from a voxel in the myocardium following CA injection contains contributions of signal change in the pre-arteriolar, arteriolar, capillary, and venular vascular components as well as interstitial space, it is unclear whether there is usable information on dispersion in the signal time curve from a myocardial voxel. To reduce the systematic error in MBF quantification due to CA dispersion, the definition of a local AIF could be envisaged.[88] The distance traveled by the CA bolus, being 1 of 2 principally decisive parameters for systematic MBF quantification errors, as found in this work, could then be corrected.

5 | CONCLUSIONS

In summary, this work presents for the first time a detailed analysis of CA flow through both left and right coronary trees down to the pre-arteriolar level using an advanced coronary-flow BC. Perfusion quantification errors evoked by observed CA dispersion show nonnegligible underestimation of MBF in dynamic CA bolus-based measurements (e.g., MRI). We expect future improvements of quantitative perfusion measurements, especially regarding spatial resolution and noise, to make systematic errors as described here more apparent in clinical perfusion data. The complexity of the process of CA transport and dispersion, as well as subsequent quantification errors, emphasizes the necessity for profound validation of CFD simulations in future studies.

ACKNOWLEDGMENTS

Financial support was obtained from the German Ministry of Education and Research (01E1O1504). This manuscript is part of Johannes Martens's Ph.D. thesis at the Julius-Maximilians University Würzburg (2019). No benefits in any form have been or will be received from a commercial party related directly or indirectly to the subject of this manuscript.

ORCID

Johannes Martens https://orcid.org/0000-0003-0170-3122
Maria Siebes https://orcid.org/0000-0002-7034-5843

REFERENCES

1. World Health Organization. The top 10 causes of death, 2016. http://www.who.int/news-room/fact-sheets/detail/the-top-10-causes-of-death. Published May 28, 2018. Accessed November 19, 2019.
2. Libby P, Theroux P. Pathophysiology of coronary artery disease. *Circulation*. 2005;111:8.
3. Hsu LY, Groves DW, Aletras AH, Kellman P, Arai AE. A quantitative pixel-wise measurement of myocardial blood flow by contrast-enhanced first-pass CMR perfusion imaging: microsphere validation in dogs and feasibility study in humans. *JACC Cardiovasc Imag*. 2012;5:154–166.
4. Bratis K, Nagel E. Variability in quantitative cardiac magnetic resonance perfusion analysis. *J Thorac Dis*. 2013;5:357–359.
5. D'Angelo T, Grigoratos C, Mazziotti S, et al. High-throughput gadobutrol-enhanced MMR: a time and dose optimization study. *J Cardiovasc Magn Reson*. 2017;19:83.
6. Schmitt M, Horstick G, Petersen SE, et al. Quantification of resting myocardial blood flow in a pig model of acute ischemia based on first-pass MRI. *Magn Reson Med*. 2005;53:1223–1227.
7. Larghat AM, Swoboda PP, Biglands JD, Kearney MT, Greenwood JP, Plein S. The microvascular effects of insulin resistance and diabetes on cardiac structure, function, and perfusion: a cardiovascular magnetic resonance study. *Eur Heart J Cardiovasc Imag*. 2014;15:1368–1376.
8. Petersen SE, Jerosch-Herold M, Hudsmith LE, et al. Evidence for microvascular dysfunction in hypertrophic cardiomyopathy: new insights from multiparametric magnetic resonance imaging. *Circulation*. 2007;115:2418–2425.
9. Jerosch-Herold M, Wilke N, Stillman AE, Wilson RF. Magnetic resonance quantification of the myocardial perfusion reserve with a fermi function model for constrained deconvolution. *Med Phys*. 1998;25:73–84.
10. Kroll K, Wilke N, Jerosch-Herold M, et al. Modeling regional myocardial flows from residue functions of an intravascular indicator. *Am J Physiol*. 1996;271:H1643–H1655.
11. King RB, Deussen A, Raymond GM, Bassingthwaighte JB. A vascular transport operator. *Am J Physiol*. 1993;265:H2196–H2208.
12. Natsume T, Ishida K, Kitagawa K, Nagata M, Sakuma H, Ichihara T. Theoretical considerations in measurement of time discrepancies between input and myocardial time-signal intensity curves in estimates of regional myocardial perfusion with first-pass contrast-enhanced MRI. *Magn Reson Imag*. 2015;33:1059–1065.
13. Xue H, Brown LAE, Nielles-Vallespin S, Plein S, Kellman P. Automatic in-line quantitative myocardial perfusion mapping: processing algorithm and implementation. *Magn Reson Med*. 2020;83:712–730.
14. Jacobs M, Benovoy M, Chang LC, Arai AE, Hsu LY. Evaluation of an automated method for arterial input function detection for first-pass myocardial perfusion cardiovascular magnetic resonance. *J Cardiovasc Magn Reson*. 2016;18:17.
15. Christian TF, Aletras AH, Arai AE. Estimation of absolute myocardial blood flow during first-pass MR perfusion imaging using a dual-bolus injection technique: comparison to single-bolus injection method. *J Magn Reson Imag*. 2008;27:1271–1277.
16. Patel AR, Antkowiak PF, Nandalur KR, et al. Assessment of advanced coronary artery disease: advantages of quantitative cardiac magnetic resonance perfusion analysis. *J Am Coll Cardiol*. 2010;56:561–569.
17. Miller CA, Naish JH, Ainslie MP, et al. Voxel-wise quantification of myocardial blood flow with cardiovascular magnetic resonance: effect of variations in methodology and validation with positron emission tomography. *J Cardiovasc Magn Reson*. 2014;16:1–15.
18. Fortin A, Salmon S, Baruthio J, Delbany M, Durand E. Flow MRI simulation in complex 3D geometries: application to the cerebral venous network. *Magn Reson Med*. 2018;80:1655–1665.
19. Boccadifuoco A, Mariotti A, Capellini K, Celi S, Salvetti MV. Validation of numerical simulations of thoracic aorta hemodynamics:

comparison with in vivo measurements and stochastic sensitivity analysis. *Cardiovasc Eng Technol*. 2018;9:688–706.
20. Condemi F, Campisi S, Viallon M, Croisille P, Fuzelier J-F, Avril S. Ascending thoracic aorta aneurysm repair induces positive hemodynamic outcomes in a patient with unchanged bicuspid aortic valve. *J Biomech*. 2018;81:145–148.
21. Mehndiratta A, Calamante F, MacIntosh BJ, Crane DE, Payne SJ, Chappell MA. Modeling and correction of bolus dispersion effects in dynamic susceptibility contrast MRI. *Magn Reson Med*. 2014;72:1762–1774.
22. Graafen D, Hamer J, Weber S, Schreiber LM. Quantitative myocardial perfusion magnetic resonance imaging: the impact of pulsatile flow on contrast agent bolus dispersion. *Phys Med Biol*. 2011;56:5167–5185.
23. Schmidt R, Graafen D, Weber S, Schreiber LM. Computational fluid dynamics simulations of contrast agent bolus dispersion in a coronary bifurcation: impact on MRI-based quantification of myocardial perfusion. *Comp Math Meth Med*. 2013;2013:513187.
24. Graafen D, Münnemann K, Weber S, Kreitner K-F, Schreiber LM. Quantitative contrast-enhanced myocardial perfusion magnetic resonance imaging: simulation of bolus dispersion in constricted vessels. *Med Phys*. 2009;36:3099–3106.
25. Sommer K, Bernat D, Schmidt R, Breit H-C, Schreiber LM. Resting myocardial blood flow quantification using contrast-enhanced magnetic resonance imaging in the presence of stenosis: a computational fluid dynamics study. *Med Phys*. 2015;42:4375–4384.
26. van den Wijngaard JPHM, Schulten H, van Horssen P, et al. Porcine coronary collateral formation in the absence of a pressure gradient remote of the ischemic border zone. *Am J Physiol Heart Circ Physiol*. 2010;300:H1930–H1937.
27. Kim HJ, Vignon-Clementel IE, Coogan JS, Figueroa CA, Jansen KE, Taylor CA. Patient-specific modeling of blood flow and pressure in human coronary arteries. *Ann Biomed Eng*. 2010;38:3195–3209.
28. Boutsianis E, Dave H, Frauenfelder T, et al. Computational simulation of intracoronary flow based on real coronary geometry. *Eur J Cardio-Thorac*. 2004;26:248–256.
29. Updegrove A, Wilson NM, Merkow J, Lan H, Marsden AL, Shadden SC. SimVascular: an open source pipeline for cardiovascular simulation. *Ann Biomed Eng*. 2017;45:525–541.
30. Sommer K, Schmidt R, Graafen D, Breit H-C, Schreiber LM. Contrast agent bolus dispersion in a realistic coronary artery geometry: influence of outlet boundary conditions. *Ann Biomed Eng*. 2013;42:787–796.
31. Martens J, Panzer S, van den Wijngaard JPHM, Siebes M, Schreiber LM. Analysis of coronary contrast agent transport in bolus-based quantitative myocardial perfusion MRI measurements with computational fluid dynamics simulations. In: Pop M, Wright GA, editors. *FIMH 2017. Volume LNCS 10263*. Toronto, Canada: Springer International Publishing; 2017. pp 369–380.
32. Itu L, Sharma P, Mihalef V, Kamen A, Suciu C, Comaniciu D. A patient-specific reduced-order model for coronary circulation. In: Proceedings of the 9th IEEE International Symposium on Biomedical Imaging, Barcelona, Spain, 2012. pp 832–835.
33. van der Horst A, Boogaard FL, Rutten MCM, van de Vosse FN. A 1D wave propagation model of coronary flow in a beating heart. In: Proceedings of the ASME Summer Bioengineering Conference, Farmington, Pennsylvania, 2011. pp 183–184.
34. Bender SB, van Houwelingen MJ, Merkus D, Duncker DJ, Laughlin MH. Quantitative analysis of exercise-induced enhancement of early- and late-systolic retrograde coronary blood flow. *J Appl Physiol*. 2010;108:507–514.
35. Kamoi S, Pretty C, Docherty P, et al. Continuous stroke volume estimation from aortic pressure using zero dimensional cardiovascular model: proof of concept study from porcine experiments. *PLoS ONE*. 2014;9:e102476.
36. Guyton AC, Hall JE. *Textbook of Medical Physiology*, 13th edn. Philadelphia, Pennsylvania: Elsevier Saunders; 2005.
37. Lelovas PP, Kostomitsopoulos NG, Xanthos TT. A comparative anatomic and physiologic overview of the porcine heart. *J Am Assoc Lab Anim*. 2014;53:432–438.
38. Kaul S, Jayaweera AR. Determinants of microvascular flow. *Eur Heart J*. 2006;27:2272–2274.
39. Layland J, Carrick D, Lee M, Oldroyd K, Berry C. Adenosine: physiology, pharmacology, and clinical applications. *JACC Cardiovasc Interv*. 2014;7:581–591.
40. Huo Y, Kassab GS. The scaling of blood flow resistance: from a single vessel to the entire distal tree. *Biophys J*. 2009;96:339–346.
41. Brinson ME, Jahn S, Nabijou H. A tabular source approach to modelling and simulating device and circuit noise in the time domain. *Int J Numer Model Electron Network Dev Field*. 2011;24:555–567.
42. Gerke E, Juchelka W, Mittmann U, Schmier J. Der intramyokardiale Druck des Hundes in verschiedenen Tiefen bei Druckbelastung und Ischämie des Herzmuskels. *Basic Res Cardiol*. 1975;70:537–546.
43. Huo Y, Kassab GS. A scaling law of vascular volume. *Biophys J*. 2009;96:347–353.
44. Kassab GS, Berkley J, Fung YCB. Analysis of pig's coronary arterial blood flow with detailed anatomical data. *Ann Biomed Eng*. 1997;25:204–217.
45. Zhou Y, Kassab GS, Molloi S. On the design of the coronary arterial tree: a generalization of Murray's law. *Phys Med Biol*. 1999;44:2929–2944.
46. Ballyk PD, Steinman DA, Ethier CR. Simulation of non-Newtonian blood flow in an end-to-side anastomosis. *Biorheology*. 1993;31:565–576.
47. Lesieur M, Metais O, Conte P. *Large-eddy simulations of turbulence*. New York, New York: Cambridge University Press; 2005.
48. Martens J, Panzer S, Van den Wijngaard J, Siebes M, Schreiber LM.Development of a computational fluid dynamics (CFD)-model of the arterial epicardial vasculature. In: Coudière Y, Ozenne V, Vigmond E, Zemzemi N, editors. *FIMH 2019. Volume LNCS 11504*. Bordeaux, France: Springer, Cham; 2019. pp 219–229.
49. Wieseotte C, Wagner M, Schreiber LM. An estimate of Gd-DOTA diffusivitiy in blood by direct NMR diffusion measurement of its hydrodynamic analogue Ga-DOTA, 2014. In: Proceedings of the Annual Meeting of ISMRM, Milan, Italy, 2014. Abstract 2618.
50. Palade GE. Blood capillaries of the heart and other organs. *Circulation*. 1961;24:368–388.
51. Mischi M, den Boer JA, Korsten HHM. On the physical and stochastic representation of an indicator dilution curve as a gamma fit. *Physiol Meas*. 2008;29:281–294.
52. Calamante F, Willats L, Gadian DG, Connelly A. Bolus delay and dispersion in perfusion MRI: implications for tissue predictor models in stroke. *Magn Reson Med*. 2006;55:1180–1185.
53. Bassingthwaighte JB. Relative dispersion: a characterizing feature of specific vascular beds. *Anesth Analg*. 1977;56:72–77.
54. Ewing JR, Bonekamp D, Barker PB. *Clinical perfusion MRI: Techniques and Applications*. Barker P, Golay X, Zaharchuk G, editors. Cambridge, United Kingdom: Cambridge University Press; 2013.

55. *MMID4 Manual: National Simulation Resource for Mass Transport and Exchange*. Seattle, Washington: Department of Bioengineering, University of Washington; 1998.
56. Jerosch-Herold M, Wilke N, Wang Y, et al. Direct comparison of an intravascular and an extracellular contrast agent for quantification of myocardial perfusion. *Int J Cardiac Imaging*. 1999;15:453–464.
57. Chan IS, Goldstein AA, Bassingthwaighte JB. SENSOP: a derivative-free solver for nonlinear least squares sensitivity scaling. *Ann Biomed Eng*. 1993;21:621–631.
58. Marquardt D. An algorithm for least-squares estimation of nonlinear parameters. *J Soc Ind Appl Math*. 1963;11:431–442.
59. Weber S, Kronfeld A, Kunz RP, et al. Quantitative myocardial perfusion imaging using different autocalibrated parallel acquisition techniques. *JMRI*. 2008;28:51–59.
60. Schmitt M, Viallon M, Thelen M, Schreiber WG. Quantification of myocardial blood flow and blood flow reserve in the presence of arterial dispersion: a simulation study. *Magn Reson Med*. 2002;47:787–793.
61. Taylor G. Dispersion of soluble matter in solvent flowing slowly through a tube. *Royal Soc A Math Phys*. 1953;219:186–203.
62. Tsuiki K, Sato Y, Sudo K, Nagasawa J. Dependency of transcoronay circulatory transport function on coronary perfusion pressure and flow. *Tohoku J Exp Med*. 1978;126:377–383.
63. Prinzen FW, Bassingthwaighte JB. Blood flow distributions by microsphere deposition methods. *Cardiovasc Res*. 2000;45:13–21.
64. Qayyum AA, Kastrump J. Measuring myocardial perfusion: the role of PET. *MRI and CT. Clin Radiol*. 2015;70:576–584.
65. Decking UKM, Pai VM, Bennett E, et al. High-resolution imaging reveals a limit in spatial resolution of blood flow measurements by microspheres. *Am J Physiol Heart Circ Physiol*. 2004;287:H1132–H1140.
66. Fluckiger JU, Benefield BC, Harris KR, Lee DC. Absolute quantification of myocardial blood flow with constrained estimation of the arterial input function. *JMRI*. 2013;38:603–609.
67. Christian TF, Rettmann DW, Aletras AH, et al. Absolute myocardial perfusion in canines measured by using dual-bolus first-pass MR imaging. *Radiology*. 2004;232:677–684.
68. Goldstein TA, Jerosch-Herold M, Misselwitz B, Zhang H, Gropler RJ, Zheng J. Fast mapping of myocardial blood flow with MR first-pass perfusion imaging. *Magn Reson Med*. 2008;59:1394–1400.
69. Schuster A, Zarinabad N, Ishida M, et al. Quantitative assessment of magnetic resonance derived myocardial perfusion measurements using advanced techniques: microsphere validation in an explanted pig heart system. *J Cardiovasc Magn Reson*. 2014;16:82.
70. Fluckiger JU, Benefield BC, Bakhos L, Harris KR, Lee DC. A comparison of theory-based and experimentally determined myocardial signal intensity correction methods in first-pass perfusion magnetic resonance imaging. *Comput Math Methods Med*. 2015;2015:843741.
71. Likhite D, Suksaranjit P, Adluru G, et al. Interstudy repeatability of self-gated quantitative myocardial perfusion MRI. *JMRI*. 2016;43:1369–1378.
72. Pontre B, Cowan BR, DiBella E, et al. An open benchmark challenge for motion correction of myocardial perfusion MRI. *IEEE J Biomed Health Inform*. 2017;21:1315–1326.
73. Schuster A, Sinclair M, Zarinabad N, et al. A quantitative high resolution voxel-wise assessment of myocardial blood flow from contrast-enhanced first-pass magnetic resonance perfusion imaging: microsphere validation in a magnetic resonance compatible free beating explanted pig heart model. *Eur Heart J Cardiovasc Imag*. 2015;16:1082–1092.
74. Bassingthwaighte JB, Malone MA, Moffett TC, et al. Molecular and particulate depositions for regional myocardial flows in sheep. *Circ Res*. 1990;66:1328–1344.
75. Decking UKM, Schrader J. Spatial heterogeneity of myocardial perfusion and metabolism. *Basic Res Cardiol*. 1999;93: 439–445.
76. Decking UKM. Spatial heterogeneity in the heart: recent insights and open questions. *News Physiol Sci*. 2002;17:246–250.
77. Bassingthwaighte JB, Beard DA, King RB. Fractal regional myocardial blood flows: the anatomical basis. In: Losa GA, Merlini D, Nonnenmacher TF, Weibel ER, eds. *Fractals in Biology and Medicine Mathematics and Biosciences in Interaction*. Basel, Switzerland: Birkhäuser; 1998:114–127.
78. Schwarz F, Hinkel R, Baloch E, et al. Myocardial CT perfusion imaging in a large animal model: comparison of dynamic versus single-phase acquisitions. *JACC Cardiovasc Imag*. 2013;6: 1229–1238.
79. Fahmi R, Eck BL, Levi J, et al. Quantitative myocardial perfusion imaging in a porcine ischemia model using a prototype spectral detector CT system. *Phys Med Biol*. 2016;61:2407–2431.
80. Ben-Haim S, Murthy VL, Breault C, et al. Quantification of myocardial perfusion reserve using dynamic SPECT imaging in humans: a feasibility study. *J Nucl Med*. 2013;54:873–879.
81. Rossi A, Uitterdijk A, Dijkshoorn M, et al. Quantification of myocardial blood flow by adenosine-stress CT perfusion imaging in pigs during various degrees of stenosis correlates well with coronary artery blood flow and fractional flow reserve. *Eur Heart J Cardiovasc Imag*. 2013;14:331–338.
82. Morton G, Chiribiri A, Ishida M, et al. Quantification of absolute myocardial perfusion in patients with coronary artery disease: comparison between cardiovascular magnetic resonance and positron emission tomography. *J Am Coll Cardiol*. 2012;60: 1546–1555.
83. Fritz-Hansen T, Hove JD, Kofoed KF, Kelbaek H, Larsson HB. Quantification of MRI measured myocardial perfusion reserve in healthy humans: a comparison with positron emission tomography. *JMRI*. 2008;27:818–824.
84. Kolandavel MK, Fruend ET, Ringgaard S, Walker PG. The effects of time varying curvature on species transport in coronary arteries. *Ann Biomed Eng*. 2006;34:1820–1832.
85. Theodorakakos A, Gavaises M, Andriotis A, et al. Simulation of cardiac motion on non-Newtonian, pulsating flow development in the human left anterior descending coronary artery. *Phys Med Biol*. 2008;53:4875–4892.
86. Zeng D, Boutsianis E, Ammann M, Boomsma K, Wildermuth S, Poulikakos D. A study on the compliance of a right coronary artery and its impact on wall shear stress. *J Biomech Eng*. 2008;130:1–11.
87. Javadzadegan A, Yong ASC, Chang M, Ng MKC, Behnia M, Kritharides L. Haemodynamic assessment of human coronary arteries is affected by degree of freedom of artery movement. *Comp Method Biomech Biomed Eng*. 2016;20:260–272.
88. Fluckiger JU, Schabel MC, DiBella EV. Toward local arterial input functions in dynamic contrast-enhanced MRI. *JMRI*. 2010;32:924–934.

SUPPORTING INFORMATION

Additional supporting information may be found online in the Supporting Information section.

VIDEO S1 Rotating coronary trees. The models of the left and right coronary arteries, segmented from the imaging cryomicrotome data set, are shown in 360°

VIDEO S2 Contrast agent flow through the rotating model of the LCT. Although a shortened bolus (factor 100) flows through the coronary tree, the model is rotated. Stripes in the CA flow are artifacts from the resolution of the underlying computational grid. The used mesh refinement is chosen based on previous benchmarking by a mesh convergence study

VIDEO S3 Contrast agent flow through the rotating model of the RCA. As in Supporting Information Video S2, a shortened bolus (factor 100) flows through the rotating RCT. Due to lower flow velocities, CA takes longer to traverse the full model, resulting in larger CA arrival times and bolus widths. The structure of the underlying computational grid may be perceptible by stripes in the CA flow. The mesh density is based on a previous mesh convergence analysis

VIDEO S4 Contrast agent flow through the vessel segment at diag3 and diag4. The CA transport takes place at a faster rate in vessels, which are oriented more favorably with regard to the preceding "mother" vessel. This leads to regionally varying CA arrival times and dispersion. At the top of the LAD, artifacts from the underlying computational grid might be visible, as in Supporting Information Videos S2 and S3

How to cite this article: Martens J, Panzer S, van den Wijngaard J, Siebes M, Schreiber LM. Influence of contrast agent dispersion on bolus-based MRI myocardial perfusion measurements: A computational fluid dynamics study. *Magn Reson Med*. 2020;84: 467–483. https://doi.org/10.1002/mrm.28125